# Supplementary Information

## Contents

# 1 Supplementary Note 1: The relationship between the holograph principle and the generalized Snell's Law.

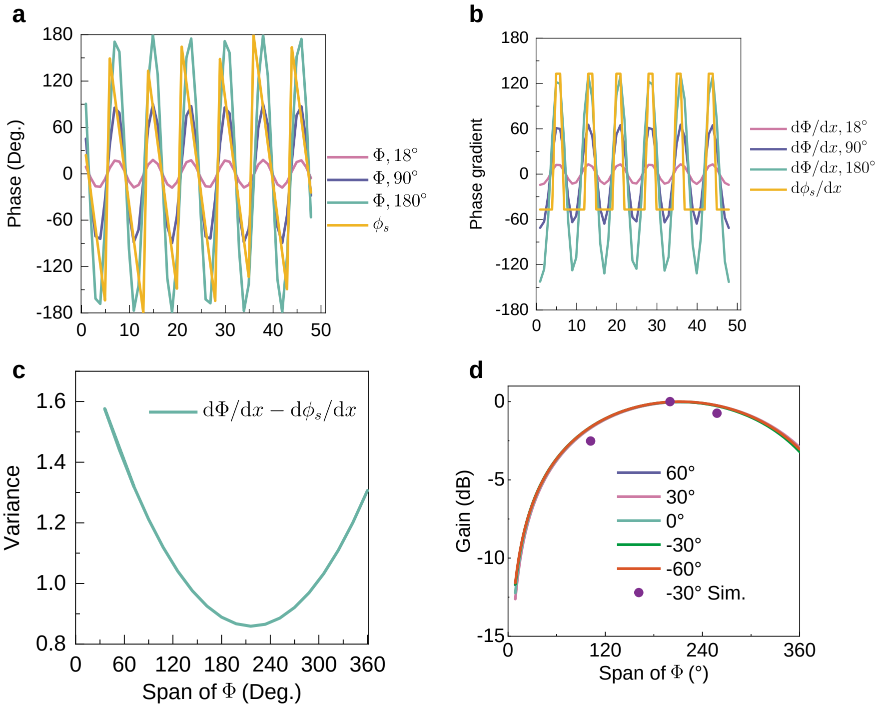

**Supplementary Figure 1.** | **a**, Phase of $\Phi$ and $\phi_s$. **b**, Phase gradient of $\mathrm{d}\Phi/\mathrm{d}x$ and $\mathrm{d}\phi_s/\mathrm{d}x$, where $\mathrm{d}\Phi/\mathrm{d}x$ is calculated when $M_{ph} = 18°$, $90°$, and $180°$. **c**, Variance of $\mathrm{d}\Phi/\mathrm{d}x - \mathrm{d}\phi_s/\mathrm{d}x$. **d**, Calculated and simulated gain when the array scans to different angles.

$$\Phi = (X_{ph} + M_{ph}\mathrm{Re}(\Phi_{\mathrm{rad}}\Phi^*_{\mathrm{surf}})) \tag{1}$$

From Equation(1) in the one-dimensional case, the amplitude of $\Phi$ rises as $M_{ph}$ increases. Curves of $\Phi$ at different values of $M_{ph}$ are presented in Supplementary Figure 1a. When $M_{ph}$ is set to 180 °, $\Phi$ and $\varphi$ share similarities. $\mathrm{d}\Phi/\mathrm{d}x$ and $\mathrm{d}\phi_s/\mathrm{d}x$ are calculated in Supplementary Figure 1b. $\mathrm{d}\Phi/\mathrm{d}x$ is the same as $\mathrm{d}\phi_s/\mathrm{d}x$ while $M_{ph}$ is 90°.

The variance of $\mathrm{d}\Phi/\mathrm{d}x - \mathrm{d}\phi_s/\mathrm{d}x$ versus the span of $\Phi$ is presented in Supplementary Figure 1c, where the span of $\Phi$ equals $2 \times |M_{ph}|$. When the span of $\Phi$ is about 211°, the variance has the lowest value. In other words, $\mathrm{d}\Phi/\mathrm{d}x$ and $\mathrm{d}\phi_s/\mathrm{d}x$ have the highest degree of similarity. At the same time, the holographic metasurface antenna reaches the highest gain, as given in Supplementary Figure 1d. It implies that when the phase gradient of a holographic antenna is close to that of an antenna based on generalized Snell's Law, the gain of a holographic antenna can be enhanced.

In this section, the derivations of generalized Snell's Law and holographic principle are also addressed for the two-dimensional case. Equation(2) presents the one-dimensional case. Equation(3) is the two-dimensional case of the generalized Snell's Law, where $r = \sqrt{x^2 + y^2}$. Equation(4) gives the $\phi_s$ from Equation(3). Equation(5) presents the phase from the Holographic principle. $\Phi$ performs a amplitude and a cosinusoidal modulation on $\phi_s$. Equation(6) gives the phase gradient of $\phi_s$. Assuming the beam direction is at $(\phi_L, \theta_L)$ in the spherical coordinate system, generalized Snell's Law and holographic principle are presented as follows:

$$kn_i \sin(\theta_i)\mathrm{d}x + (\phi_s + d\phi_s) = kn_t \sin(\theta_L)\mathrm{d}x + \phi_s \tag{2}$$

$$\begin{aligned}
kn_i\mathrm{d}r + (\phi_s + d\phi_s) &= kn_t \sin(\theta_L)\cos(\phi_L)\mathrm{d}x + kn_t \sin(\theta_L)\sin(\phi_L)\mathrm{d}y + \phi_s && (3)\\
\phi_s &= kn_t \sin(\theta_L)\cos(\phi_L)x + kn_t \sin(\theta_L)\sin(\phi_L)y - kn_i r && (4)\\
\Phi &= X_{ph} + M_{ph}\cos(kn_t \sin(\theta_L)\cos(\phi_L)x + kn_t \sin(\theta_L)\sin(\phi_L)y - kn_i r)\\
&= X_{ph} + M_{ph}\cos(\phi_s) && (5)\\
\frac{\mathrm{d}\phi_s}{\mathrm{d}x} &= kn_t \sin(\theta_L)\cos(\phi_L) - \frac{kn_i x}{r} && (6)\\
\frac{\mathrm{d}\Phi}{\mathrm{d}x} &= -M_{ph}(kn_t \sin(\theta_L)\cos(\phi_L) - \frac{kn_i x}{r})\\
&\quad \sin(kn_t \sin(\theta_L)\cos(\phi_L)x + kn_t \sin(\theta_L)\sin(\phi_L)y - kn_i r)\\
&= -M_{ph}\sin(\phi_s)\frac{\mathrm{d}\phi_s}{\mathrm{d}x} && (7)
\end{aligned}$$

From Equation(5) and (7), in the two-dimensional case, the holographic principle can also be regarded as a modulated form of generalized Snell's Law.

## 2 Supplementary Note 2: Simulated patterns of surface impedance modulated antenna, phase modulated antenna, and reflectarray fed by an horn.

$$\Phi = (X_{ph} + M_{ph}\mathrm{Re}(\Phi_{\mathrm{rad}}\Phi^*_{\mathrm{surf}})) \tag{8}$$

The holographic antenna constructed by surface impedance is given in Supplementary Figure 2a. For comparison, a phased-modulated holographic antenna based on Equation(8) is shown in Supplementary Figure 2b. These two holographic antennas are fed by a probe in the center, providing surface waves. The simulated results are presented in Supplementary Figure 2c. The patterns are almost the same, validating the phased-modulated method.

Concurrently, this element can also serve to constitute a reflective antenna(Supplementary Figure 2d). The reflected phase of the elements in the

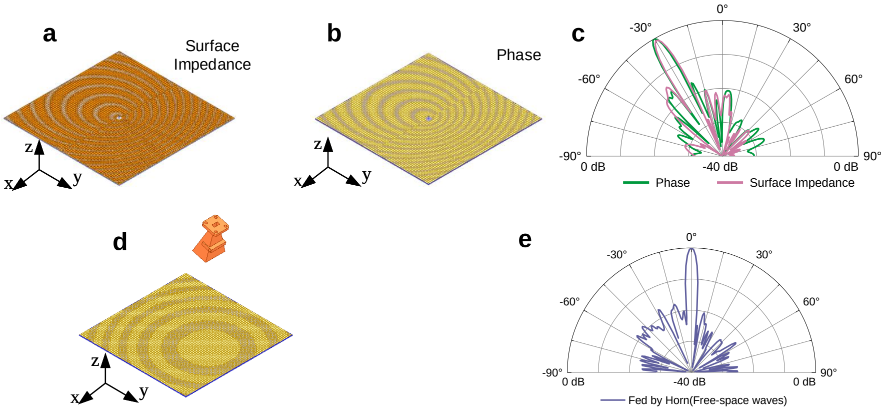

**Supplementary Figure 2.** | **The principle of SFC antennas.a**,Surface impedance modulated antenna excited by surface waves. **b**,Phase modulated antenna fed by surface waves. **c**,Simulated radiation patterns for the two antennas. **d**,Reflectarray fed by an horn. **e**,Simulated radiation pattern of the reflectarray.

antenna is given as:

$$\varphi(x_t) = k\left(|\vec{r}_{x_t} - \vec{r}_{\text{feed}}| - \vec{r}_{x_t} \cdot \hat{u}\right) + \varphi_0 \tag{9}$$

where $\varphi(x_t)$ is a reflected phase of the element on the XOY plane, $\vec{r}_{x_t}$ is a radius vector, $\vec{r}_{\text{feed}}$ is a phase center's position vector of the horn, $\hat{u}$ is a beam direction vector, $\varphi_0$ is introduced for design freedom. Supplementary Figure 2e depicts the simulated radiation pattern, where a beam in the broadside direction is generated.

## 3 Supplementary Note 3: Calculated maximum gain at other scan angles versus different $\varphi_m$ and $\varphi_0$.

Supplementary Figure 3 depicts the calculated maximum gain versus different $\varphi_m$ and $\varphi_0$. The gain is normalized to 0 dB. When the beam is steered to (30°,0°) and (−30°,0°), the symmetrical property results in nearly identical patterns. When the scan angle increases from 0° to 60 °, the influence of $\varphi_0$ on gain is decreasing. With regard to $\varphi_m$, a midpoint value can enhance the gain.

## 4 Supplementary Note 4: Simulated radiated patterns using different state distributions.

Supplementary Figure 4 demonstrates simulated patterns from different phase distributions. In Supplementary Figure 4a, the distribution 1 contains state ’00’ and ’01’. State ’00’ and ’11’ are utilized in Supplementary Figure 4b. The radiated patterns are shown in Supplementary Figure 4c. The patterns are almost the same. Compared with state ’00’ and ’01’, state ’00’ and ’01’ exhibits an analogous proficiency in the modulation of free-space waves. In Supplementary Figure 4d, only state ’00’ and ’10’ are

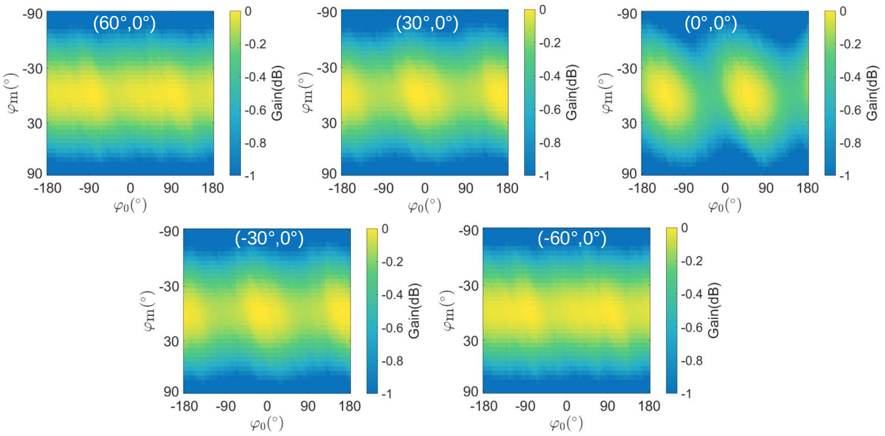

**Supplementary Figure 3.** |Calculated maximum gain at other scan angles versus different $\varphi_m$ and $\varphi_0$, when free-space waves feed the array.

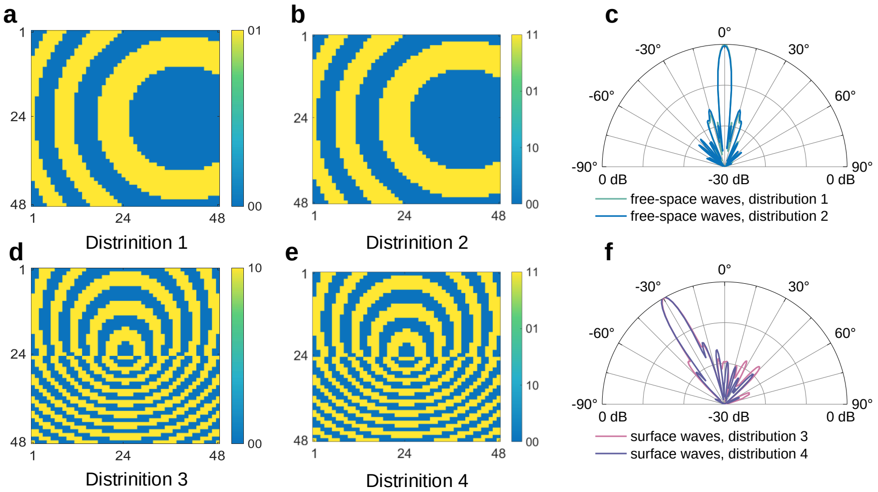

Distrinition 1

Distrinition 2

Distrinition 3

Distrinition 4

**Supplementary Figure 4.** |**a**, Distribution 1: state '00' and '01'. **b**, Distribution 2: state '00' and '11'. **c**, Simulated radiated patterns when free-space waves feed the array. **d**, Distribution 3: state '00' and '10'. **e**, Distribution 3: state '00' and '11'. **f**, Simulated radiated patterns when the array is excited by surface waves.

used. State '00' and '11' are deployed in Supplementary Figure 4e for modulating the surface waves. The simulated patterns are illustrated in Supplementary Figure 4f. We observe that state '10' and '11' have similar ability of manipulating the surface waves.

## 5 Supplementary Note 5: States distribution at different $\Phi_1$ and $\Phi_2$ in the circularly polarized SFC metasurface antenna.

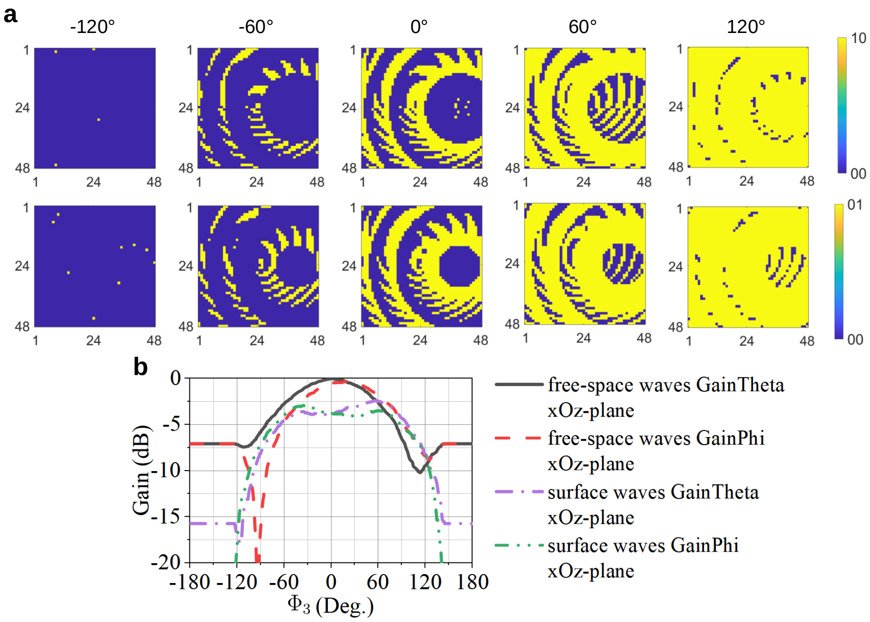

**Supplementary Figure 5.** |**a**, State distributions at different quantized angles. **b**, Calculated normalized gain at different quantized angles where $\Phi_1 = \Phi_2 = \Phi_3$.

In Supplementary Figure 5a, state distributions at different quantized angles are presented. With the quantized angle increasing, State '10' and State '01' occupy more and more space in the state distribution. When the value of quantized angle is less than $-60°$ and larger than $60°$, the pattern is indistinct. Indistinct distribution will deteriorate the radiated patterns from surface waves and free-space waves. As shown in Supplementary Figure 5b, the gain drops a lot when the quantized angle is larger than $120°$ or less than $-120°$. When $\Phi_3$ is $0°$, the gain of free-space waves reaches its peak value. The gain of surface waves has its peaks at about $-60°$ and $60°$. Considering that identical gains from surface waves and free-space waves contribute to the robustness of the system, the values near $-60°$ are recommended. After optimization, the quantized value is set to $-51°$ for verification. When the quantized value is near $60°$, the increasing coupling between the elements deteriorates the performance.

## 6 Supplementary Note 6: Other details in near-field and far-field.

Supplementary Figure 6a presents the simulated near-field electric distribution when the SFC is fed by surface waves. The electric distribution concentrates on the center. Supplementary Figure 6b illustrates the near-field distribution when the SFC is excited

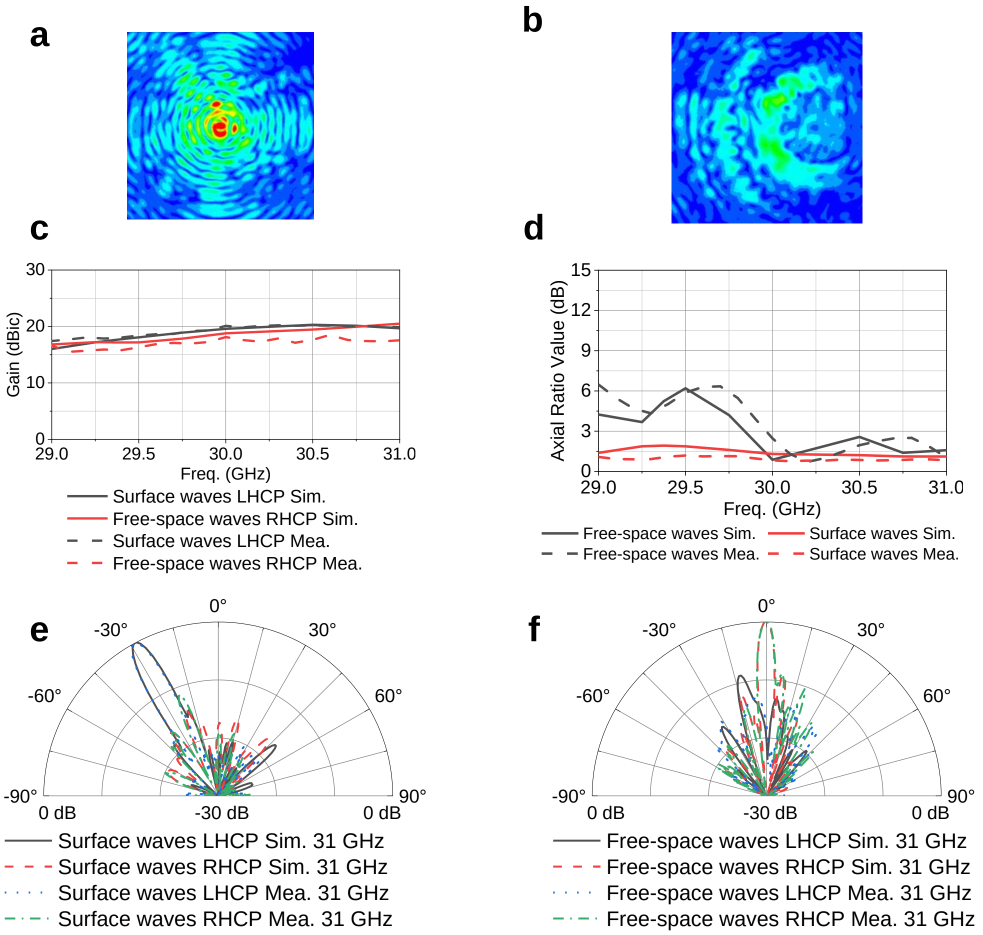

**Supplementary Figure 6.** |**a,** Simulated near-field electric distribution when the SFC is fed by surface waves. **b,** Simulated near-field electric distribution when the SFC is fed by free-space waves. **c,** Simulated and measured gain when surface waves and free-space waves feed the array, respectively. **d,** Simulated and measured axial ratio versus frequency. **c,** The simulated and measured radiated patterns when surface waves excite the SFC metasurface antenna at 31 GHz. **d,** The simulated and measured radiated patterns when free-space waves excite the SFC metasurface antenna at 31 GHz.

by free-space waves. The electric field is predominantly concentrated on the right side and diverges in a pattern akin to concentric circles. The simulated and measured gains from surface waves and free-space waves are presented in Supplementary Figure 6c. Upon the gain from surface waves, the measured and simulated results agree well. The measured gain from free-space waves is lower than the simulated gain. The potential reasons include manufacturing errors and mounting errors. In Supplementary Figure

6d, the simulated and measured results of axial ratio(AR) are presented. At 30 GHz, the AR is slightly higher than the simulated results when free-space waves feed the antenna. The AR stays below 3 dB within the frequency range from 30 to 31 GHz, indicating that a circularly polarized beam is radiated. When the SFC metasurface is excited by surface waves, the measured AR remains below 3 dB from 29 to 31 GHz, where Left Hand Circle Polarization(LHCP) are emitted into free space. The radiated patterns at 31 GHz are presented in Supplementary Figure 6e and Supplementary Figure 6f, respectively. The simulated and measured results are in good agreement.

## 7 Supplementary Note 7: Simulated and measured S-parameter.

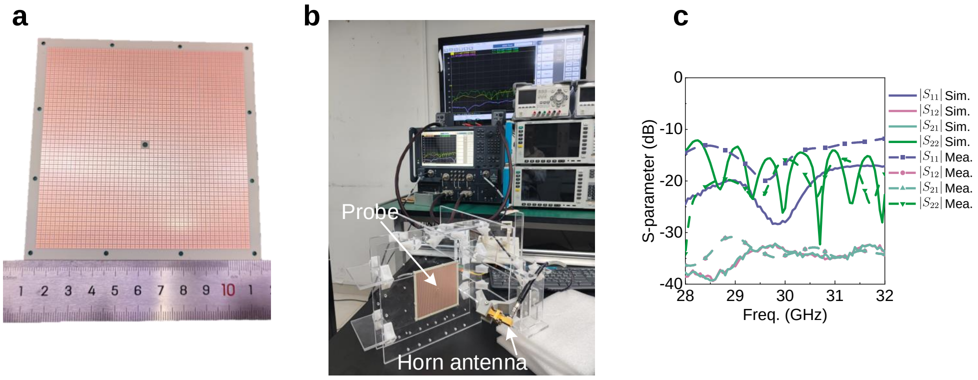

**Supplementary Figure 7.** |**a**, A Photo of the metasurface. **b**, An image depicting the experimental setup for the measurement process. **c**, Simulated and measured S-parameters.

Supplementary Figure 7a presents a photo of the proposed metasurface. A test photo is given in Supplementary Figure 7b. The S-parameters are measured using a network analyzer configured in two-port test mode. One is linked to a probe to excite surface waves. Another one is connected to a horn antenna for generating free-space waves. The simulated and measured results are demonstrated in Supplementary Figure 7c. The reflected coefficients of surface waves and free-space waves are consistently kept below $-10$ dB within 28-32 GHz. The measured reflected coefficients are still less than $-10$ dB from 28 to 32 GHz. The isolation between them is higher than 30 dB across 28-32 GHz. The measured isolation agrees well with the simulated results.